Materials Science and Engineering Faculty
Research & Creative Works

Materials Science and Engineering

10 Jul 2023

Calibration Of The Johnson–Cook Model At High Temperatures For An Ultra-High Strength CrNiMoV Steel

Mario F. Buchely
Missouri University of Science and Technology, buchelym@mst.edu

S. Chakraborty

V. Athavale

Laura Bartlett
Missouri University of Science and Technology, lnmkvf@mst.edu

et. al. For a complete list of authors, see *https://scholarsmine.mst.edu/matsci_eng_facwork/3188*

Recommended Citation

Calibration of the Johnson–Cook model at high temperatures for an Ultra-High Strength CrNiMoV Steel

M.F. Buchely [a],[*], S. Chakraborty [a], V. Athavale [a], L. Bartlett [a], R. O'Malley [a], D. Field [b], K. Limmer [b], K. Sebeck [c]

[a] *Department of Materials Science and Engineering, Missouri S&T, Rolla, MO 65409, USA*
[b] *U.S. Army Combat Capabilities Development Command Army Research Laboratory, 6300 Rodman Rd., Aberdeen Proving Ground, MD 21005, USA*
[c] *US Army DEVCOM Command Ground Vehicle Systems Center, USA*

ARTICLE INFO

ABSTRACT

This paper presents a study on the thermo-mechanical behavior of an ultra-high strength CrNiMoV steel at high temperatures and medium strain rates through hot tensile tests. The material was examined in two conditions: as-cast/heat-treated (AC/HT) and as-rolled (AR). Tensile tests were conducted at temperatures of $800, 900, 1000, 1100,$ and 1200 °C, and strain rates of $0.1, 1,$ and 10 s^{-1}. Inclusion and porosity analysis was also performed on the tensile specimens. The results revealed that the flow stress decreased by approximately 70% on average from 800 °C to 1200 °C, while increasing by approximately 32% on average from 0.1 s^{-1} to 10 s^{-1} in strain rate. The elongation exhibited an increase from 16.5% at 800 °C to 33% at 1200 °C. However, the ductility transition was slower than expected, particularly for the AC/HT conditions. The AC/HT samples exhibited higher levels of inclusions and porosity compared to the AR samples, with porosity significantly affecting the elongation to failure and ultimate tensile strength (UTS) at a strain rate of 1 s^{-1}. Furthermore, calibrated Johnson–Cook parameters were reported and compared, demonstrating excellent agreement between predicted and experimental values with less than 20% variation. The calibrated Johnson–Cook model can be effectively employed for modeling purposes within the studied temperature range, and its application can even be extrapolated for higher strain rates.

1. Introduction

Ultra-high strength steels are of increasing interest in weight-critical applications where a reduction in thickness can be supported by an increase in strength. These types of steels possess attractive characteristics of hardness and toughness for such applications, with a minimum yield strength of 1380 MPa (200 ksi) [1,2]. Various steel types fulfill these requirements, including martensitic steels, dual-phase steels, TRIP steels, and bainitic steels, among others. Quenched and tempered (Q&T) martensitic high-strength steels are well-established alloys designed to control martensitic transformation and produce alloys with high hardenability [3,4]. This enables the achievement of a fully martensitic microstructure, even at slower cooling rates. Many grades have been explored, such as CrMo, CrMoV, CrNiMo, CrNiMoV, and CrNiMoW alloys, which are considered highly alloyed steels [1,5]. One example of these alloys is the AF9628 steel [6,7].

Numerous studies have been conducted on Q&T steels, with a particular focus on the impact of heat treatment [8,9]. These investigations have sought to enhance the strength-toughness properties of such steels by employing various heat treatment approaches [10,11]. Of particular interest is the tempering stage, which follows the quenching process and plays a crucial role in improving the material's ductility while preserving its hardness to a significant extent. This enhancement is achieved through carbon segregation from the supersaturated martensite matrix, leading to the formation of small carbides, typically in the form of ϵ carbides, which contribute to hardness retention [12]. Tempering temperatures for low and medium carbon steels typically range from 100 °C to 250 °C. However, it should be noted that higher tempering temperatures may induce temper martensite embrittlement (TME), potentially compromising the final mechanical properties of the steel [13].

Highly alloyed steels pose a significant challenge due to the presence of segregation in their microstructure, which hampers their processability using conventional techniques like forging and hot rolling [14]. However, a comprehensive understanding of the behavior of these steels under conditions of high temperatures and medium strain rates is key to overcoming these technical challenges.

Nomenclature

$\bar{\sigma}$	Mean flow stress (MFS) during rolling
Δh	Rolling draft, thickness difference
$\dot{\epsilon}$	Uniaxial strain-rate
$\dot{\epsilon}_0$	JC strain-rate of reference
$\dot{\epsilon}_m$	Plane strain-rate during rolling
ϵ	Uniaxial strain
ϵ_m	Plane strain during rolling
σ	Uniaxial stress
σ_Y	Uniaxial yield stress
σ_{uts}	Uniaxial ultimate tensile strength
A	JC material parameter
B	JC material parameter
C	JC material parameter
C_H	Parameter in the Hitchcock equation
$elong(\%)$	Elongation in uniaxial tensile test
F	Rolling forces
h_0	Initial thickness of the rolled plate
h_f	Final thickness of the rolled plate
h_m	Mean thickness of rolled plate
L'_p	corrected arc of contact during rolling
m	JC material parameter
n	JC material parameter
p_r	Rolling pressure
R	Radius of rolls
R'	Corrected radius of rolls
T	Temperature
T^*	JC non-dimensional temperature
T_{melt}	JC material melting temperature
T_{ref}	JC temperature of reference
v_r	Linear velocity of the rolling plate
w_m	Mean width of rolled plate

Table 1
Chemical composition (in wt.%) of studied alloy.

Condition	C	Mn	Cr	Si	Ni	Mo	V	N ppm	S ppm	P ppm
AC/HT	0.28	0.55	2.80	0.92	1.04	1.04	0.10	< 100	< 65	< 65
AR	0.26	0.62	3.11	1.06	0.97	1.16	0.11	< 80	< 15	< 65

AC/HT: As-Cast/Heat-treated, AR: As-Rolled.

The Johnson–Cook (JC) strength model is a well-known relation extensively used for modeling and simulating metal-mechanical process interactions. This model provides a straightforward relationship among stress (σ), strain (ϵ), strain rate ($\dot{\epsilon}$), and non-dimensional temperature (T^*), as shown below:

$$\sigma = (A + B\epsilon^n)\left(1 + C \ln \frac{\dot{\epsilon}}{\dot{\epsilon}_0}\right)\left(1 - T^{*m}\right) \tag{1}$$

Here, A, B, n, C, and m are material parameters, $\dot{\epsilon}0$ is a reference strain rate, and the non-dimensional temperature is calculated using two reference temperatures. Typically, these reference temperatures are chosen as the lowest testing temperature ($Tref$) and the melting point of the material (T_{melt}), as expressed by the following equation:

$$T^* = \frac{T - T_{ref}}{T_{melt} - T_{ref}} \tag{2}$$

In this paper, the mechanical behavior of a CrNiMoV alloy at high temperatures is studied. To accomplish this, hot tensile tests were conducted, and the material flow stress was fitted to the established Johnson–Cook flow model. Additionally, the model was verified and validated using hot rolling tests and experimental compression data obtained from Lillo et al. [16].

2. Materials and methods

The alloy was studied in two conditions: in the heat treated, as-cast stage (AC/HT) and after hot rolling (AR). Target chemical compositions for both conditions are displayed in Table 1.

The as-cast steel was prepared utilizing charge materials including Induction Iron (99.9%Fe), ferro-chrome, ferro-moly, and others. The melting was done in a 200 lb core-less induction furnace, air-melted but flowing argon to cover and protect the melt. The heat was tapped at 1650 °C into a 200 lb capacity teapot-style ladle. Aluminum shot was added during tapping to deoxidize the steel in the ladle. The melt was poured into a phenolic no-bake sand mold to form Y-blocks with dimensions 176 mm × 178 mm × 53 mm (∼ 90 kg). Previous casting experience in our foundry has shown that heat treatment of the casting is necessary to minimize segregation and improve mechanical properties [18,19]. Thus, sections from the bottom of the Y block were utilized for heat treatment using the following steps: (i) Hydrogen bake at 320 °C for 6 hrs, (ii) Normalization at 1110 °C for 4 hrs followed by air cooling, and (iii) Sub-critical anneal at 650 °C for 4 hrs followed by air cooling [11,20]. For the wrought product, the alloy was vacuum induction melted and cast into ingots. The ingots were subsequently hot rolled at 1250 °C. A total thickness reduction of 73% was applied in the ingots to produce 20 mm thick plates.

Tensile specimens were prepared from the AC/HT blocks and from the AR plates according to the ASTM E8-16 standard, sub-size specimen No. 3 (see Fig. 1). First, blocks were sectioned by Electrical Discharge Machining (EDM), and then turning in round specimens. From the AR plates, longitudinal (L) and transverse (T) to the rolling directions samples were extracted and characterized independently.

Tensile testing was performed using a servo-hydraulic MTS frame equipped with a high temperature furnace. Details of this test can be found in the previously published article by Buchely et al. [17]. Thermal cycling is schematically shown in Fig. 2a. First, material was heated to 1200 °C at 80 °C/min and held for 2 min, in order to
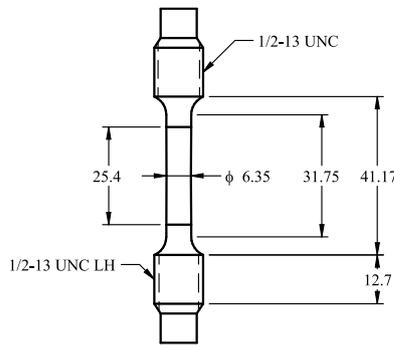
Specifically, the flow stress, recrystallization mechanisms, and microstructural changes at elevated temperatures need to be thoroughly investigated [15]. By gaining insights into these aspects, it becomes possible to develop effective strategies for processing and optimizing the performance of highly alloyed steels in demanding applications.

Most of the literature on Q&T high-strength steels focuses on the mechanical characterization of these steels at room or medium temperatures (below 300 °C). Some data is available for this type of steel at high temperatures (above 800 °C), but only under quasi-static conditions. Lillo et al. [16] studied the AF9628 alloy to develop potential rolling schedules. In their study, compression tests were conducted at temperatures ranging from 950 °C to 1050 °C and true strain rates up to 10 s^{-1} were applied for material characterization. However, further studies are required to verify and replicate these results. This is particularly important for adapting this material to forging and rolling modeling purposes. It is worth noting that forging and rolling practices are performed at temperatures ranging from 800 °C to 1250 °C within the austenite phase field. Therefore, characterizing the material at these temperatures is crucial for appropriate improvement and optimization of hot deformation processes in this type of steel.

In a previous study [17], the authors conducted an extensive characterization of various steels at high temperatures, with a specific focus on rolling applications. In that study, the Johnson–Cook strength model was fully characterized. However, it is important to note that most of the steels considered in that study were intended for structural applications, and the properties of high-strength steels may differ under different temperature and strain rate conditions.

Fig. 1. Hot tensile specimen: Schematic of sub size No. 3 (ASTM E8-16).

dissolve precipitates and homogenize the starting material. After that, temperature was decreased to the testing temperature and held for 5 min to obtain stable and constant temperature, before testing. Upon conclusion of the test, the material was air cooled in the frame. Tests were performed at different temperatures from 800 °C to 1200 °C, and different strain-rates from 0.1 s^{-1} to 10 s^{-1}.

After testing from different testing conditions, specimens were metallographically prepared according to ASTM E3-11 standard. Microstructures were evaluated by optical microscopy (OM) and scanning-electron microscopy (SEM). Additionally, some samples were prepared for non-metallic inclusion and porosity analysis, by sectioning the tested specimen close to the breaking point, as shown in Fig. 2b.

An SEM (ASPEX PICA 1020) with energy dispersive X-ray spectroscopy (EDS), and automated feature (AFA) was used to characterize the size, composition, and distribution of the non-metallic inclusions, as well as to determine the area fractions of the inclusions. Inclusion analysis was carried out with a beam voltage of 20 keV and 1000X magnification for all the samples using a completely randomized statistical method, in-built with the SEM/EDS software. Previous work showed this instrument is accurate method to characterize inclusions as smaller as 0.5 μm [21,22].

Porosity measurement was carried out with the same beam energy, but lower magnification (200X) for selected samples following the same completely randomized statistical method. Estimated areas of different inclusions and porosity were normalized by the scanning area of each samples and this was represented as area fraction (ppm), as described by Chakraborty et al. [23].

Johnson–Cook strength parameters (A, B, n, C, and m) were calibrated using the true stress — plastic strain experimental tensile curves by Genetic Algorithms optimization, as described by Buchely et al. [24].

To validate the JC model, a lab scale hot-rolling test was performed using an instrumented STANAT rolling mill in a 2-high configuration using 5 inches diameter rolls. This equipment was described in previous papers [25,26]. For this validation test, an AC/HT block (64 mm thick × 64 mm wide × 76 mm long) was hot rolled at high ($\sim$ 1200 °C) and low temperatures ($\sim$ 900 °C) to reduce the thickness of the block down to 12.5 mm thick. Rolling forces were collected during different rolling passes, and then compared to rolling forces predicted using the JC model according to the Green–Wallace model, as follows:

$$p_r = \frac{\bar{\sigma}}{2} \left(\frac{L'_p}{h_m} + \frac{h_m}{L'_p} \right) \tag{3}$$

where p_r is the rolling pressure, $\bar{\sigma}$ is the mean flow stress (MFS) during rolling, h_m is the mean thickness, $L'_p = \sqrt{R'\Delta h}$ is the corrected arc of contact during rolling, R' is the corrected radius of the rolls, and Δh is the thickness difference.

Rolling pressures can be approximated as follows:

$$p_r = \frac{F}{w_m L'_p} \tag{4}$$

where F is the rolling force, and w_m is the mean block width. To calculate L'_p, R' is approximated using the Hitchcock equation, as follows:

$$R' = R \left(1 + \frac{2C_H F}{w_m \Delta h} \right) \tag{5}$$

where C_H is a constant depending of the type of rolls ($C_H = 8.35$ E − 8 in2/lbf for steel rolls). Additionally, MFS can be calculated using JC equation Eq. (1), as follows:

$$\bar{\sigma} = \frac{\sqrt{3}}{2} \left(A + \frac{B\epsilon_m^n}{1+n} \right) \left(1 + C \ln \frac{\dot{\epsilon}_m}{\dot{\epsilon}_0} \right) \left(1 - T^{*m} \right) \tag{6}$$

where $\epsilon_m = \ln(h_0/h_f)$ is the plane strain during rolling, $\dot{\epsilon}_m = v_r \sqrt{\frac{1}{L'_p \Delta h}} \epsilon_m$ is the plane strain-rate during rolling, v_r is the linear velocity of the rolling plate, and h_0, h_f are the initial and final block thickness during rolling. In Eq. (6), the $\frac{\sqrt{3}}{2}$ factor comes from the conversion of uniaxial stress to plane strain condition [27].

After combining previous equations, and some mathematical simplification, rolling force is calculated as follows:

$$F \left(1 - C_H \bar{\sigma} \frac{R}{h_m} \right) = \frac{w_m \bar{\sigma}}{2} \left(\frac{\Delta h R}{h_m} + h_m \right) \tag{7}$$

This equation is used to calculated theoretical rolling force, and then compared to the experimental rolling force obtained during rolling.

3. Results

Figs. 3a and 3b show the microstructure of the AC/HT material after heat treatment. The microstructure is martensitic with small bainitic regions (see black arrow in 3b). Notice that even after normalization, segregation and the remnants of the dendritic structure from casting is still observable the microstructure. Additionally, the micrographs can be utilized to determine the large prior-austenite grain size PAGs (PAG boundary as white arrows in figures), which is on the order of millimeters. High level of porosity was also observed (circles in 3a).

Figs. 3c and 3d show the microstructure of the AR material after deformation. The microstructure consists of a fully martensite matrix, and PAGs were observed in the range of 50–100 μm. Notice the banding in the steel due to the hot-rolling.

3.1. Hot tensile test

Figs. 4–6 show the engineering and true stress–strain curves generated from the hot tensile test at different temperatures (between 800 °C to 1200 °C) and different strain-rates (between 0.1 s^{-1} to 10 s^{-1}). Ranges of temperature and strain-rate were selected accordingly to industrial hot rolling practices [28]. Additionally, Table 2 summarized the main tensile properties for the tested material at each experimental conditions. As expect, the flow stress increases at the higher strain-rate and the flow stress decreases as the temperature increases. Elongation also is higher at higher temperatures. It should be noted that the yield stress is not affected by the starting material condition; however, the elongation seems to be lower for the AC/HT material. The UTS of the AC/HT samples is also lower; this is especially more pronounced in the 1 s^{-1} rate test as compared to the AR samples.

3.2. Inclusion and porosity analysis

Figs. 7 and 8 show a conjoined ternary diagram of the inclusion population within the samples after tensile testing for the AC/HT, AR-L and AR-T conditions. In general the AC/HT condition samples showed a larger number of inclusions, including alumina, manganese sulfide, complex inclusion (alumina + manganese sulfide), and silicates. Manganese sulfides and complex inclusions were barely observed in the AR-L and AR-T conditions.
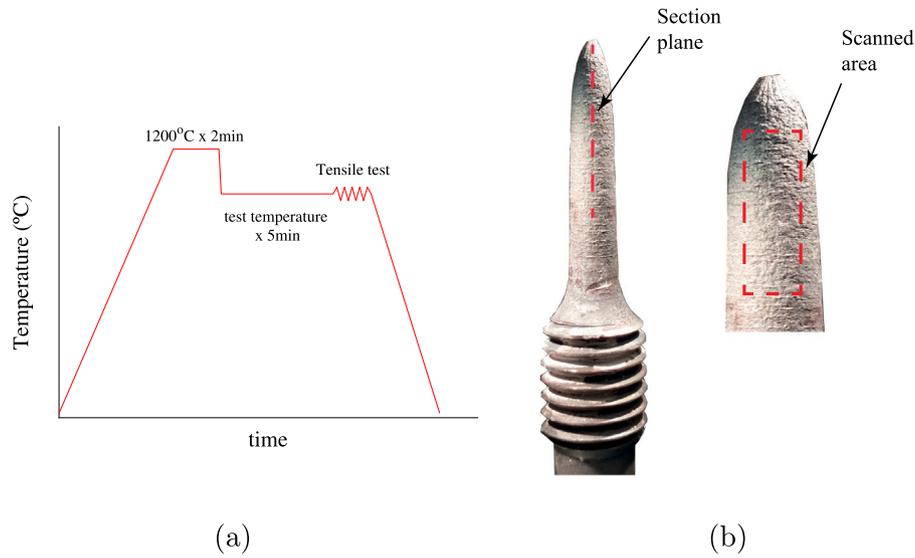
Fig. 2. Tensile test and analysis: (a) Thermal profile for hot tensile test, and (b) Specimen after tensile test, sectioning and scanned area for inclusions and porosity analysis.
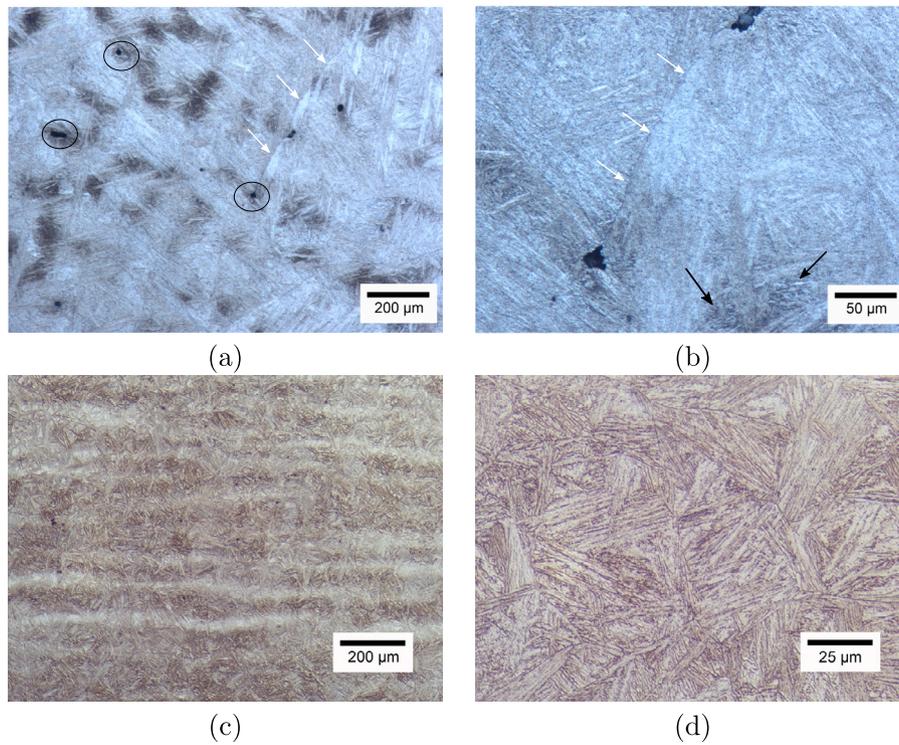

Fig. 3. Initial microstructure of studied material: (a) and (b) AC/HT material, and (c) and (d) AR material in the rolling direction.

Table 2
Summary of hot tensile properties in tested materials at different conditions. Standard deviations for different variable: elong. $\pm 4\%$, $\sigma_Y \pm 18$ MPa, $\sigma_{uts} \pm 54$ MPa.

$\dot{\varepsilon}$	T	$(elong(\%)$ - $\sigma_Y(MPa)$ - $\sigma_{uts}(MPa))$		
(s^{-1})	(°C)	AC/HT	AR-L.	AR-T.
1	800	16.9–83.0–206.2	19.1–83.1–236.3	19.9–87.5–241.3
1	900	22.6–76.5–154.6	24.3–76.5–171.3	24.7–79.3–172.1
1	1000	24.1–58.2–112.1	30.1–61.3–129.7	31.4–61.1–130.2
1	1100	30.1–40.7–76.2	30.8–47.6–94.1	32.8–48.6–96.9
1	1200	30.9–25.7–52.1	33.3–29.3–60.5	32.0–29.8–60.3
0.1	900	24.9–69.5–137.9	27.0–63.5–128.0	30.7–62.4–131.9
10	900	20.6–88.4–200.7	22.3–83.3–212.1	21.4–83.1–212.3

Area fractions of different inclusions are shown in Fig. 9. As discuss previously, higher area fractions of inclusions were observed in the AC/HT condition for all analyzed temperatures. Count of porosity was also measured for each prepared sample, and the results are shown in Fig. 10. On average, higher area fraction of porosity were observed in the AC/HT samples. This would be expected when comparing an as-cast to wrought structure. Hot working is well known to act as a method to heal void damage and close porosity.

3.3. Johnson–Cook model calibration

Table 3 shows the calibrated parameters for the JC strength model of the different material states. Fig. 11 shows the comparison between
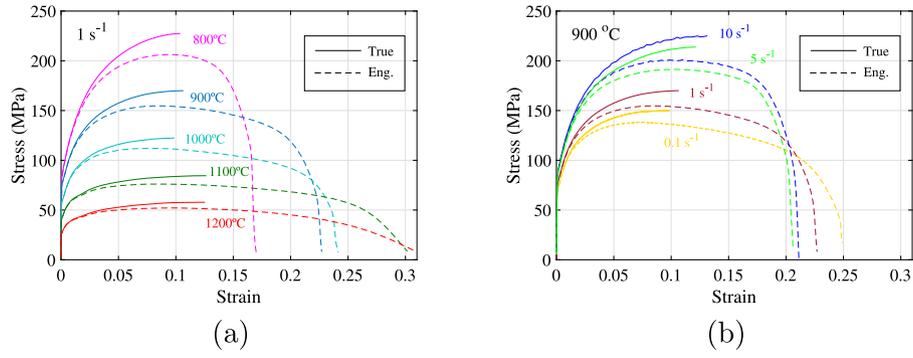
Fig. 4. Engineering and True stress–stress curves for AC/HT material: (a) Effect of temperature at 1 s^{-1}, and (b) effect of strain-rate at 900 °C.
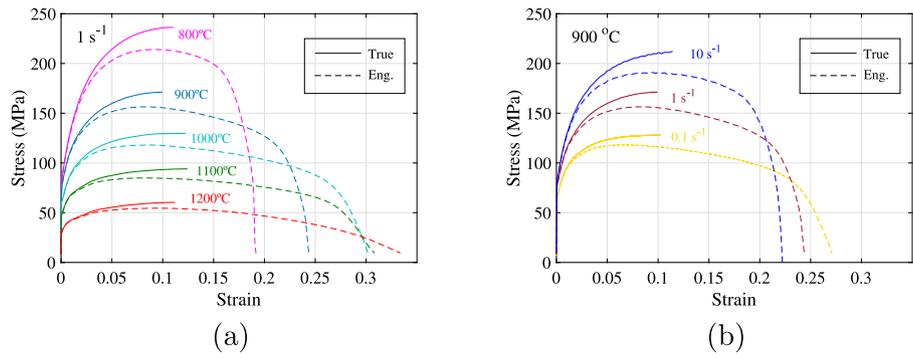

Fig. 5. Engineering and True stress–stress curves for AR material, longitudinal direction (AR-L): (a) Effect of temperature at 1 s^{-1}, and (b) effect of strain-rate at 900 °C.
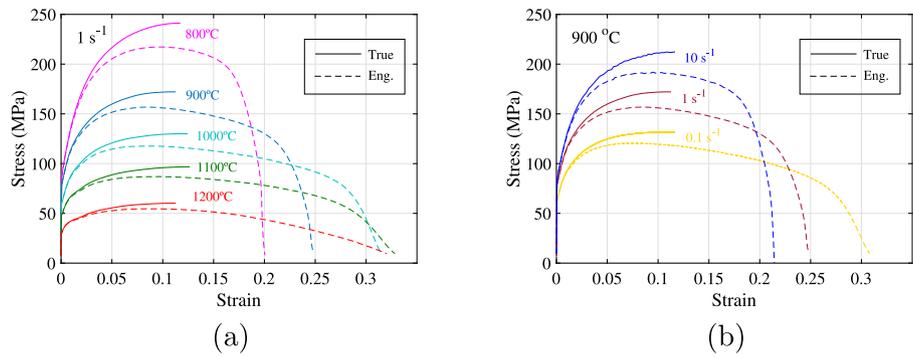

Fig. 6. Engineering and True stress–stress curves for AR material, transverse direction (AR-T): (a) Effect of temperature at 1 s^{-1}, and (b) effect of strain-rate at 900 °C.
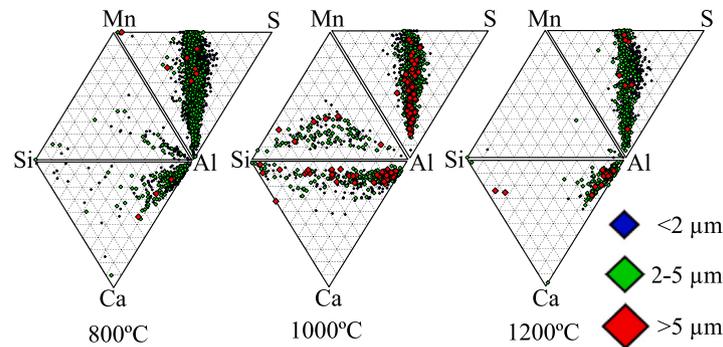

Fig. 7. Inclusion analysis: Ternary diagrams from tensile specimen from AC/HT condition at three different testing temperatures.
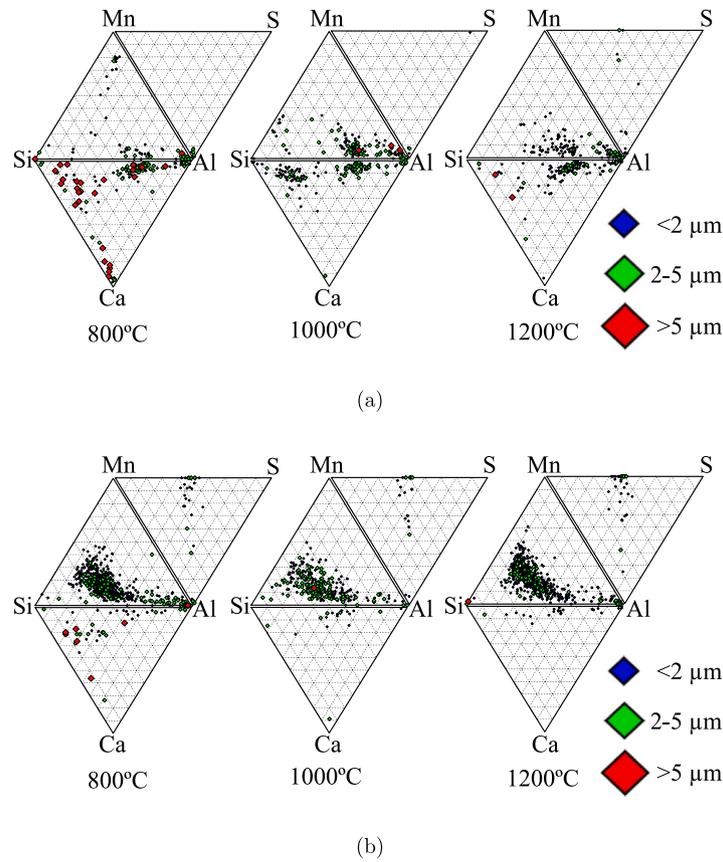
Fig. 8. Inclusion analysis: Ternary diagrams from tensile specimen from (a) AR-L, and (b) AR-T conditions, at three different testing temperatures.
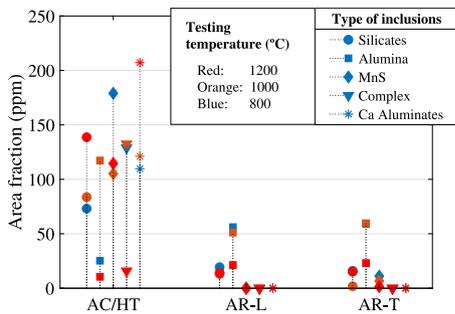

Fig. 9. Area fractions of different types of inclusions for different material conditions and at different testing temperatures.
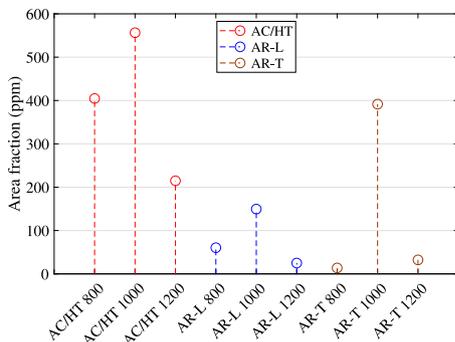

Fig. 10. Porosity area fraction for different material conditions and at different testing temperatures.

Table 3
Calibrated JC parameters for different material conditions.

	A (MPa)	*B* (MPa)	*n*	*C*	*m*	$\dot{\epsilon}_0$	T_{ref}
AC/HT	51.71	216.11	0.3555	0.1021	0.6468	0.0779	900
AR-L.	57.75	187.95	0.3346	0.0977	0.6665	0.0797	900
AR-T.	55.81	177.36	0.3340	0.1200	0.6621	0.0767	900

experimental data and predicted stress using calibrated parameters and the JC strength equation (Eq. (1)). Good agreement were found when comparing predicted and experimental flow stresses in the different materials.

3.4. Johnson–Cook model verification

Fig. 12 shows the results of the rolling trials in the AC/HT studied material. Fig. 12a shows the schedule of the rolling process, where 12 passes where performed at high temperature (above 1150 °C) and set of three final passes at lower temperatures (below 950 °C). During the rolling after every pass, the width and thickness of the rolled plate was measured, and the plastic strain was calculated as $\epsilon_m = \ln(h_0/h_f)$. The calculated plastic strain per pass is also shown in Fig. 12a. A max of 0.2 strain per pass was achieved in the lab scale rolling trail, which is an expected level of reduction in breakdown mills during hot rolling of slabs. Fig. 12b shows the comparison between the experimental forces measuring during the rolling trail, and the calculated forces using the calibrated JC model and Eq. (7).

4. Discussion

Fig. 13 shows the phase predictions upon cooling calculated using JMatPro, based on an average composition between the AC/HT and
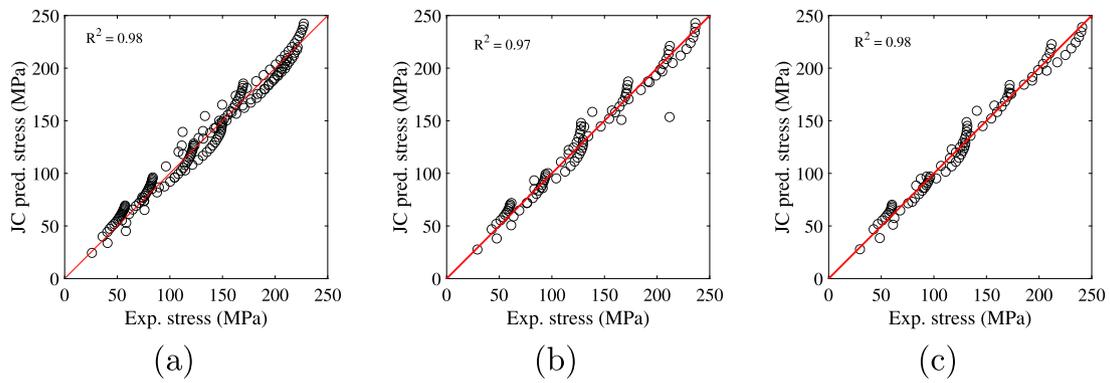
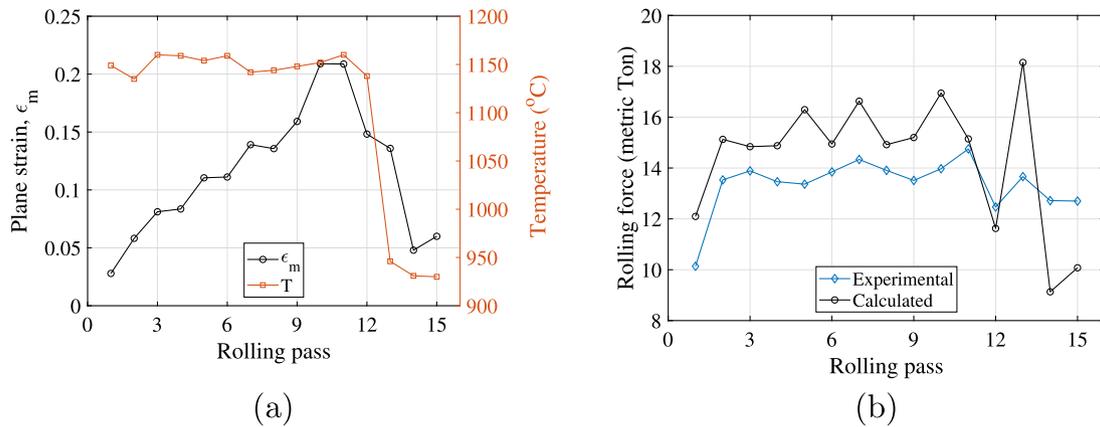**Fig. 11.** Comparison of measured stress and predicted stress using JC equation.

Fig. 12. Results from rolling trails using STANAG rolling mill: (a) summary of strain ϵ_m and temperatures T per pass, and (b) comparison between measured and calculated rolling forces.
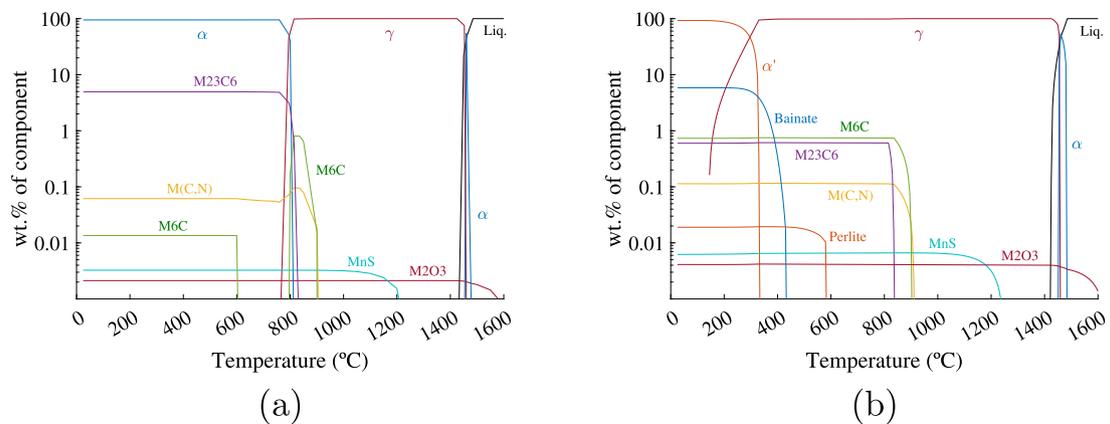

Fig. 13. Prediction of phases upon cooling calculated by JMatPro: (a) equilibrium phase stability diagram and (b) calculated microstructural component diagram under constant cooling at 0.1 °C/s. Notice that the vertical axis is in Log scale.

AR steel. Under equilibrium conditions, ferrite is predicted as the main phase at room temperature (Fig. 13a). However, when a slow continuous cooling rate of 0.1 °C/s is considered in the calculation, martensite becomes the primary structure calculated at room temperature, with a small amount of bainite present (Fig. 13b). This second prediction aligns with the observed microstructure of the material (Fig. 3). Considering the slow cooling rate used in the calculation (0.1 °C/s), this prediction highlights the high hardenability of the alloy, which is expected for this particular material.

Based on the thermodynamic modeling presented in Fig. 13a, it was anticipated that the initial heating of the steel alloy to 1200 °C would dissolve the majority of the second-phase particles prior to testing.

However, it should be noted that according to the same modeling, carbides and nitrides could theoretically re-precipitate in the matrix within the temperature range, particularly M(C, N) and M23C6, as also discussed by Zhou et al. [29]. These particles are expected to act as pinning particles when formed at dislocation cores or grain boundaries, which in turn can have an impact on the ductility and yield stress of the material.

Figs. 14a and 14b present the elongation and yield stress data, respectively, obtained from Table 2 as a function of testing temperatures. Generally, above 1000 °C, the changes in elongation are less pronounced compared to the changes observed below 1000 °C. Conversely, the change in yield stress is more significant above 900 °C
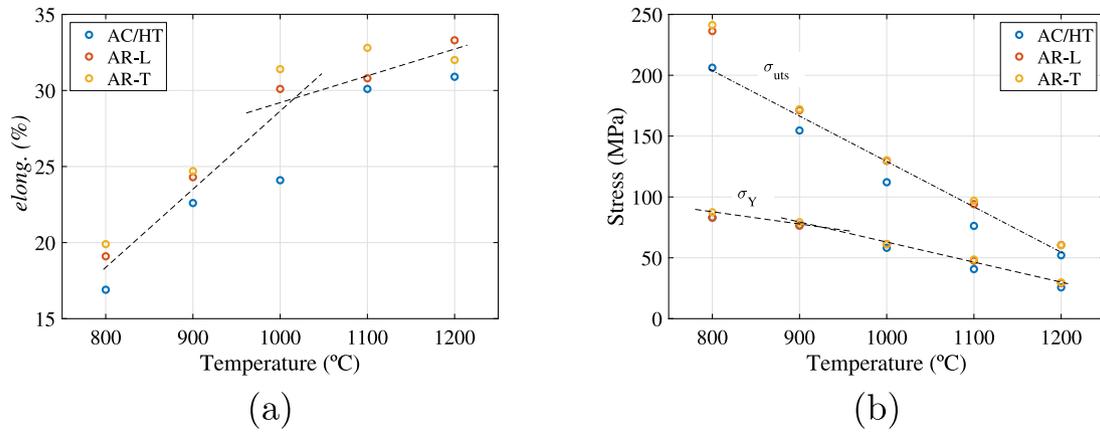
Fig. 14. Comparison of experimental tensile data among different temperatures (from Table 2): (a) comparison of elongation, and (b) comparison of yield stress (σ_Y) and ultimate strength stress (σ_{uts}). The blue dot at 1000 °C in (a) represents the data point with the highest porosity fraction (see Fig. 10) and has been excluded from the proposed linear interpolation shown by the segmented line in the plot. (For interpretation of the references to color in this figure legend, the reader is referred to the web version of this article.)
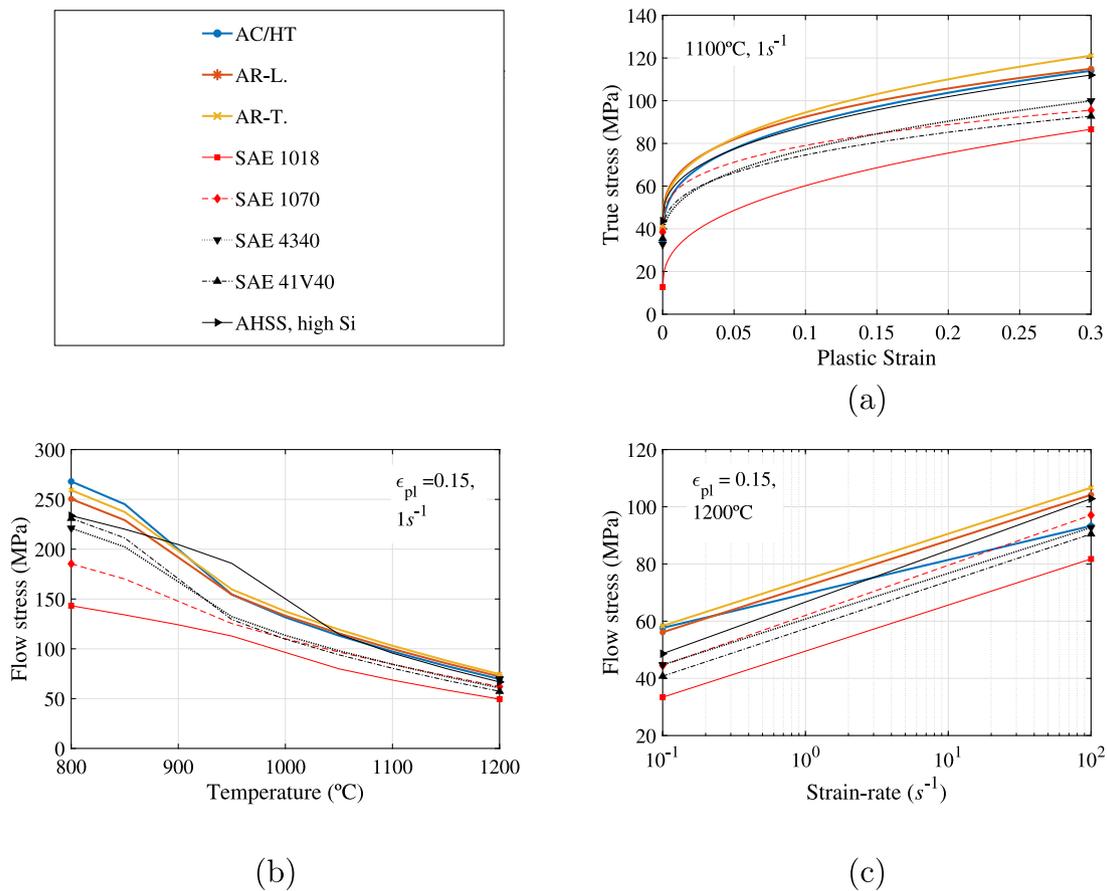

Fig. 15. Comparison of JC strength predictions for different steels [17]: (a) Stress–strain curves at 1100 °C, 1 s⁻¹, (b) Effect of temperature in the flow stress at fixed plastic strain $\epsilon_{pl} = 0.15$ and 1 s⁻¹, and (c) Effect of strain-rate in the flow stress at fixed plastic strain $\epsilon_{pl} = 0.15$ and 1200 °C. (For interpretation of the references to color in this figure legend, the reader is referred to the web version of this article.)

than below this temperature. The significant transition observed at 900 °C can potentially be attributed to the precipitation of second-phase particles during the test, which leads to a reduction in ductility as well as a shift in the flow behavior of the alloy.

It is also observed that the ductility and stresses consistently lower for the AC/HT samples. This result can be explained by the greater occurrence of non-metallic inclusions observed within the AC/HT samples, which is understood to be a function of air-melting versus vacuum-melting the alloy. Of significant note is the degraded elongation of the AC/HT sample tested at 1000 °C (indicated by the blue dot at 1000 °C

in Fig. 14a). However, the authors would like to draw the readers' attention back to Fig. 10, where it was observed that the 1000 °C sample had the highest measured porosity among all the surveyed samples, which affected the final sample ductility. The root cause of the elevated measured porosity is potentially associated with the sampling site within the bulk of the casting and is not considered to be correlated to the testing event.

By comparing the ternary diagrams of the inclusion distribution (Figs. 7 and 8), it becomes evident that there is a higher percentage of inclusions in the air-induction melted AC/HT condition compared
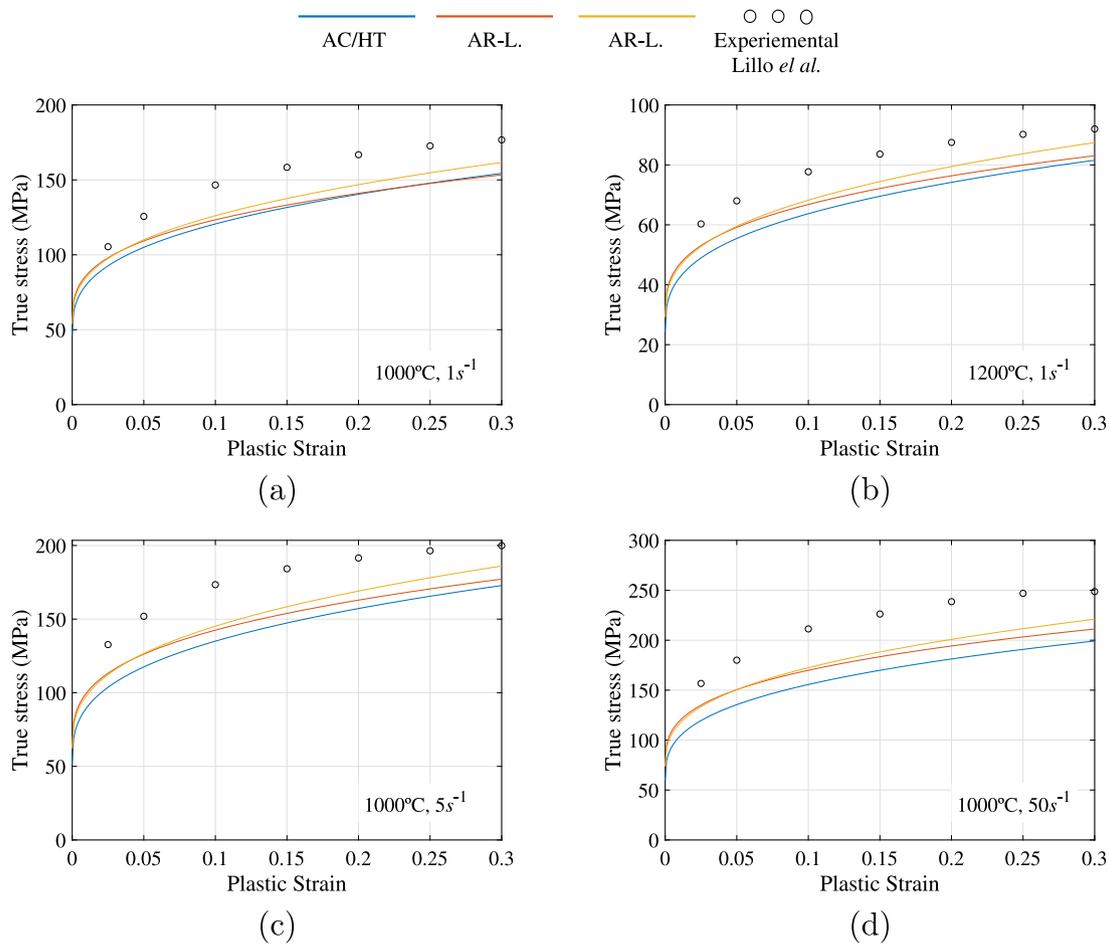
Fig. 16. Stress–Strain curve comparisons between model and experimental data from Lillo et al. [16]. Solid lines represent the calculated curves using the calibrated JC model in this paper, and circle markers represent the experimental data from literature. (a) 1000 °C, 1 s^{-1}, (b) 1175 °C, 1 s^{-1}, (c) 1000 °C, 5 s^{-1}, and (d) 1000 °C, 50 s^{-1}. (For interpretation of the references to color in this figure legend, the reader is referred to the web version of this article.)

to the vacuum-induction melted AR condition. This difference is attributed to the cleanliness of the two different heats, particularly the sulfur levels, as well as the presence of oxygen and nitrogen, which can be entrained into the melt during pouring in an open-air environment. The AC/HT material exhibited sulfur levels of approximately 65 ppm, whereas the AR material showed sulfur levels of approximately 12 ppm. Despite the difference in inclusion populations, it appears that the plastic flow behavior of the steel is not significantly affected, as similar stress levels were obtained after the tensile tests under different conditions (Fig. 14b). However, the inclusions may have an impact on the ductility and elongation to failure of the steel, where higher inclusion levels seem to result in lower ductility (Fig. 14a). This observation is consistent with previous studies on ultra-high strength steels, where the presence of inclusions did not significantly affect the strength levels but substantially reduced the steel's toughness at higher inclusion volume fractions and smaller inclusion spacings [3,30].

Compared to other steels (see Table 4) [17], the currently studied CrNiMoV steel exhibits higher flow stresses at different temperatures and strain rates. Fig. 15 compares the flow stress at 15% plastic strain among different steels as a function of temperature. At higher temperatures, the differences are less significant due to the dissolution of carbon-nitrides, as explained previously.

Compared to a similar material studied in the literature by Lillo et al. [16], experimental data from compression tests conducted on a CrNiMoV alloy at similar temperatures and strain rates are presented. The selected data from this reference is plotted in Fig. 16 using circle markers. In the same plots, the Johnson–Cook (JC) models with calibrated parameters for each condition (Table 3) are also shown. It is

worth noting that similar trends were obtained for each case, including the extrapolated condition of 50 s^{-1}, which was not experimentally tested in this current work. On average, the differences between the data and the predictions are less than 20%, which falls within acceptable engineering controls for prediction. The variations in the response values could be attributed to the different types of tests performed. In this work, uniaxial tensile data was used for characterization, while Lillo et al. utilized compression plane-strain data. The differences between these types of tests theoretically relate to $\frac{\sqrt{3}}{2}$ (see Eq. (6)), which is close to the observed differences of 20% in this comparison. Given that the sets of experimental data were independently determined, it is demonstrated that the calibrated JC models in this work are well-established and can be utilized for modeling purposes within the temperature range and even for higher (extrapolated) strain rates.

5. Conclusions

This study investigated the mechanical behavior of a CrNiMoV alloy under two different conditions: as-cast and heat treated (AC/HT) and as-hot rolled (AR). Hot tensile tests were conducted at temperatures ranging from 800 °C to 1200 °C and strain rates ranging from 0.1 s^{-1} to 10 s^{-1}, and the material response at the range of temperatures and strain rates was calibrated using the Johnson–Cook flow model. Several key findings have emerged from this research.

1. It was observed that the AC/HT condition exhibited higher levels of inclusions and porosity compared to the AR condition. This discrepancy had a significant impact on the elongation and

Table 4
Chemical composition of different steel grades [17].

Grade	C	Mn	Si	S	P	Nb	V	Cu	Ni	Cr	Mo
SAE 1018	0.16	0.60	0.18	0.02	0.01	–	–	0.02	–	–	< 0.02
SAE 1070	0.71	0.73	0.53	0.02	0.01	< 0.01	–	0.17	0.05	0.13	0.03
SAE 4340	0.42	0.77	0.26	0.01	0.04	–	–	0.25	1.82	0.74	0.26
SAE 41V40	0.40	1.27	0.23	0.02	0.02	–	0.09	0.27	0.12	0.73	0.26
AHSS, High Si	0.18	2.60	1.90	0.01	0.01	< 0.01	< 0.01	0.02	< 0.01	0.04	< 0.01

ultimate tensile strength (UTS) levels, particularly at a strain rate of 1 s^{-1}. However, it should be noted that the yield and flow stress (up to 10% plastic strain) appeared to be similar between the AC/HT and AR conditions. This indicates that while the presence of inclusions and porosity may affect certain mechanical properties, it does not significantly impact the overall deformation behavior in terms of yielding and flow stress.

2. The calibrated Johnson–Cook (JC) models for the CrNiMoV alloy demonstrated good agreement with experimental data within the temperature range of 800 °C to 1200 °C, and even for higher (extrapolated) strain rates up to 50 s^{-1}. The reliability of the calibrated JC models was confirmed through comparison with in-house hot rolling trials and independent experimental data obtained from other researchers. This suggests that the developed JC models can be effectively utilized for modeling purposes during hot deformation processes such as rolling and forging, where the alloy experiences elevated temperatures and varying strain rates.

3. In comparison to other commonly used alloys within the same range of temperatures and strain rates, the investigated CrNiMoV alloy exhibited superior flow stresses. These findings emphasize the importance of carefully selecting appropriate thermal processing conditions for the CrNiMoV steel to prevent excessive loads on rolling and forging machinery. Furthermore, further investigations are warranted to explore the influence of recrystallization and prior-austenitic grain size on the flow stress at high temperatures in this steel. A deeper understanding of these factors will contribute to optimizing the thermal processing and enhancing the performance of the CrNiMoV alloy in demanding applications.

4. This study provides valuable insights into the mechanical behavior of the CrNiMoV alloy under different conditions and contributes to the understanding of its response during hot deformation. The findings highlight the importance of considering inclusion and porosity effects on elongation and UTS levels, while also demonstrating the applicability of the calibrated JC models for simulating and predicting material behavior in relevant temperature and strain rate regimes.

CRediT authorship contribution statement

M.F. Buchely: Conceptualization, Methodology, Validation, Formal analysis, Investigation, Writing – original draft, Visualization. **S. Chakraborty:** Data curation, Formal analysis, Writing- Original draft, Visualization. **V. Athavale:** Visualization, Investigation. **L. Bartlett:** Writing – review & editing, Project administration, Funding acquisition. **R. O'Malley:** Conceptualization, Supervision. **D. Field:** Conceptualization, Supervision, Writing – review & editing. **K. Limmer:** Project administration. **K. Sebeck:** Supervision.

Declaration of competing interest

The authors declare that they have no known competing financial interests or personal relationships that could have appeared to influence the work reported in this paper.

Data availability

Data will be made available on request.

Acknowledgments

References

[1] T. Philip, T. McCaffrey, Ultrahigh-strength steels, in: ASM Handbook, in: Properties and Selection: Irons, Steels, and High-Performance Alloys, vol.1, ASM International, 1990, p. 12.

[2] C.R. Hasbrouck, A.S. Hankey, R. Abrahams, P.C. Lynch, Sub-surface microstructural evolution and chip formation during turning of AF9628 steel, in: 48th SME North American Manufacturing Research Conference, NAMRC 48, 2020, pp. 559–569.

[3] W.M. Garrison, Ultrahigh-strength steels for aerospace applications, JOM 42 (5) (1990) 20–24, http://dx.doi.org/10.1007/BF03220942.

[4] L. Keränen, M. Kangaspuoskari, J. Niskanen, Ultrahigh-strength steels at elevated temperatures, J. Construct. Steel Res. 183 (2021) http://dx.doi.org/10.1016/j.jcsr.2021.106739.

[5] Y. Sun, J. Quan, H. Salvador, J. Edwards, J. Lin, T. Kozmel, S. Mathaudhu, Ausforming and tempering of a novel ultra-high strength steel, Mater. Sci. Eng. A 838 (2022) 142750, http://dx.doi.org/10.1016/j.msea.2022.142750.

[6] R.A. Abrahams, Low Alloy High Performance Steel, 2019, p. 21, US Patent 10,445,621 B2.

[7] V. Sinha, M. Gonzales, R.A. Abrahams, B.S. Song, E.J. Payton, Correlative microscopy for quantification of prior austenite grain size in AF9628 steel, Mater. Charact. 159 (August 2018) (2020) 109835, http://dx.doi.org/10.1016/j.matchar.2019.109835.

[8] G. Krauss, Ch. 18. Deformation, mechanical properties, and fracture of quenched and tempered carbon steels, in: Steels : Processing, Structure, and Performance, ASM International, 2015.

[9] G. Sahoo, K.K. Singh, V. Kumar, Quenched and tempered high strength steel: A review, J. Met. Mater. Miner. 30 (4) (2020) 19–29, http://dx.doi.org/10.14456/jmmm.2020.47.

[10] D.M. Field, S.R. Cluff, K.R. Limmer, J.S. Montgomery, D.J. Magagnosc, K.C. Cho, Heat treatment and austenitization temperature effect on microstructure and impact toughness of an ultra-high strength steel, Metals 11 (5) (2021) 723, http://dx.doi.org/10.3390/met11050723.

[11] D.M. Field, J.S. Montgomery, K.R. Limmer, K. Cho, Heat treatment design to modify the martensite misorientation and obtain superior strength–toughness combinations, Metall. Mater. Trans. A 51 (3) (2020) 1038–1043.

[12] G. Krauss, Heat treated martensitic steels: Microstructural systems for advanced manufacture, ISIJ Int. 35 (4) (1995) 349–359, http://dx.doi.org/10.2355/isijinternational.35.349.

[13] J.P. Materkowski, G. Krauss, Tempered martensite embrittlement in SAE 4340 steel, Metall. Trans. A 10 (11) (1979) 1643–1651, http://dx.doi.org/10.1007/BF02811697.

[14] B.G. Thomas, J.K. Brimacombe, I.V. Samarasekera, The formation of panel cracks in steel ingots: A state-of-the-art review, II. Mid-face and off-corner cracks, Trans. Iron Steel Soc. 7 (10) (1986) 7–20.

[15] V.B. Ginzburg, Metallurgical design of flat rolled steels, in: Manufacturing Engineering and Materials Processing, Marcel Dekker, Inc., 2005.

[16] T.M. Lillo, J.A. Simpson, J.K. Walleser, Summary of Gleeble-based, High Temperature Deformation Study on AF9628 Steel, TARDED Technical Report No. OPSEC#1980, Idaho National Laboratory, 2019.

[17] M.F. Buchely, S. Ganguly, D.C. Van Aken, R. O'Malley, S. Lekakh, K. Chandrashekhara, Experimental development of Johnson–Cook strength model for different carbon steel grades and application for single-pass hot rolling, Steel Res. Int. 91 (7) (2020) 1–10.

[18] T.O. Webb, D.C. Van Aken, S.N. Lekakh, Evaluating chemical homogeneity in the performance of Eglin steel, in: Proceedings of the 118th Metal Casting Congress, AFS, Schaumburg, IL, USA, 2014.

[19] V. Athavale, D. Aken, M. Xu, Effect of deoxidation and pouring practice on the mechanical properties of stage-I tempered Cr-Ni-Mo steel, in: Proceedings of the 123rd Metal Casting Congress, AFS, Atlanta GA, USA, 2019.

[20] V. Athavale, T. Yaniak, M. Xu, D. Van Aken, Mechanical properties and impact wear resistance of 540 Brinell hardness Mn-Si-Mo-V steel, in: Proceedings of the 123rd Metal Casting Congress, AFS, Atlanta GA, USA, 2019.

[21] S. Chakraborty, R.J. O'Malley, L. Bartlett, M. Xu, Removal of alumina inclusions from molten steel by ceramic foam filtration, Int. J. Metalcast. 15 (3) (2021) 1006–1020.

[22] S. Chakraborty, R.J. O'Malley, L. Bartlett, Ceramic foam filter micropores as sites for liquid inclusion retention, Int. J. Metalcast. (2021).

[23] S. Chakraborty, R.J. O'Malley, L. Bartlett, M. Xu, Efficiency of solid inclusion removal from the steel melt by ceramic foam filter: Design and experimental validation, in: AFS Transactions, vol. 126, 2018, pp. 325–333.

[24] M.F. Buchely, X. Wang, D.C. Van Aken, R.J. O'Malley, S.N. Lekah, K. Chandrashekhara, The use of genetic algorithms to calibrate Johnson-Cook strength and failure parameters of AISI/SAE 1018 steel, J. Eng. Mater. Technol. 141 (2) (2019) 12.

[25] M.F. Buchely, D.M. Field, D.C. Van Aken, Analysis of hot-and cold-rolled loads in medium-Mn TRIP steels, Metall. Mater. Trans. B 50 (3) (2019) 1180–1192.

[26] M.F. Buchely, X. Wang, D.C. Van Aken, R.J. O'Malley, S. Lekakh, K. Chandrashekhara, Rolling pressures during the hot-roll of three different steel plates: Experimental, theoretical and FEA, in: Proceedings of 2nd International Symposium on the Recent Developments in Plate Steels, AIST, June 3-6, 2018, Orlando, FL, 2018, p. 10.

[27] E. Orowan, The calculation of roll pressure in hot and cold flat rolling, Proc. Inst. Mech. Eng. 150 (1) (1943) 140–167.

[28] Y.V.R.K. Prasad, K.P. Rao, S. Sasidhar, Hot Working Guide: A Compendium of Processing Maps, second ed., ASM international, 2015.

[29] T. Zhou, R.P. Babu, Z. Hou, J. Odqvist, P. Hedström, Materialia precipitation of multiple carbides in martensitic CrMoV steels - experimental analysis and exploration of alloying strategy through thermodynamic calculations, Materialia 9 (2020) 100630, http://dx.doi.org/10.1016/j.mtla.2020.100630.

[30] J.W. Bray, J.L. Maloney, K.S. Raghavan, W.M. Garrison, A comparison of the fracture behavior of two commercially produced heats of HY180 steel differing in sulfide type, Metall. Trans. A 22 (10) (1991) 2277–2285, http://dx.doi.org/10.1007/BF02664993.